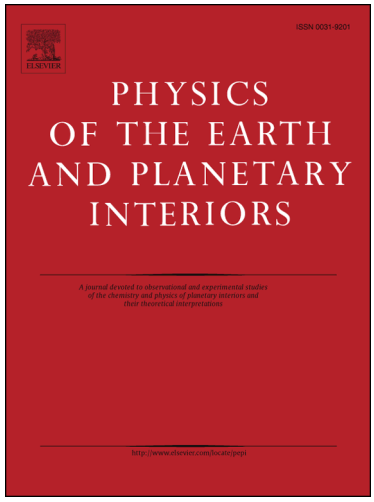

The inner core hemispheric boundary near 180°W

Wen-che Yu, Jun Su, Teh-Ru Alex Song, Hsin-Hua Huang, Laetitia Mozziconacci, Bor-Shouh Huang

PII: S0031-9201(17)30189-9
DOI: http://dx.doi.org/10.1016/j.pepi.2017.09.002
Reference: PEPI 6081

To appear in: *Physics of the Earth and Planetary Interiors*

Received Date: 27 May 2017
Revised Date: 2 September 2017
Accepted Date: 3 September 2017

Please cite this article as: Yu, W-c., Su, J., Song, T.A., Huang, H-H., Mozziconacci, L., Huang, B-S., The inner core hemispheric boundary near 180°W, *Physics of the Earth and Planetary Interiors* (2017), doi: http://dx.doi.org/10.1016/j.pepi.2017.09.002

The inner core hemispheric boundary near 180°W

Wen-che Yu[a,*] (Email: fgsyw@earth.sinica.edu.tw),

Jun Su[b] (Email: 103602009@cc.ncu.edu.tw),

Teh-Ru Alex Song[c] (Email: alex.song@ucl.ac.uk),

Hsin-Hua Huang[a] (Email: hhhuang@earth.sinica.edu.tw),

Laetitia Mozziconacci[d] (Email: laetitia@ntou.edu.tw),

and Bor-Shouh Huang[a] (Email: hwbs@earth.sinica.edu.tw)

[a] Institute of Earth Sciences, Academia Sinica, No. 128, Section 2, Academia Road, Nangang, Taipei, 11529, Taiwan

[b] Department of Earth Sciences, National Central University, No. 300, Jhongda Road, Jhongli, Taoyuan, 32001, Taiwan

[c] Department of Earth Sciences, University College London, Gower Street, London, WC1E 6BT, United Kingdom

[d] Institute of Applied Geosciences, National Taiwan Ocean University, No. 2 Beining Road, Zhongzheng, Keelung, 20224, Taiwan

*Corresponding author.

Wen-che Yu

Institute of Earth Sciences, Academia Sinica, No. 128, Section 2, Academia Road, Nangang, Taipei, 11529, Taiwan

Email: fgsyw@earth.sinica.edu.tw; Telephone: 886-2-2783-9910 ext. 311; Fax: 886-2-2783-9871

Revised for *Physics of the Earth and Planetary Interiors*

Abstract

The inner core (IC) east–west hemispheric dichotomy is widely recognized, but the reported position of the hemispheric boundary varies among studies due to uneven sampling coverage and the data analyzed. This study investigates the sharpness of the western hemispheric boundary (WHB) near 180°W by analyzing differential time residuals of PKiKP–PKPdf and PKP(bc–df) for PKPdf phases that sample 155°E–130°W in various azimuthal directions. Using PKiKP–PKPdf observations, the WHB is located at 175°E–180°W in the southern hemisphere, based mainly on the lateral isotropy–anisotropy transition. However, based on the lateral isotropic velocity contrast and this isotropy–anisotropy transition between the two hemispheres, its location is 170–160°W in the northern hemisphere. These findings indicate that the WHB is sharp and exhibits a latitudinal dependence with a 10°–20° kink, as well as 1.75% anisotropy in the uppermost IC across the 180–155°W range of the western hemisphere. As suggested by PKP(bc–df), the WHB could remain at 160°W at depth. The isotropic velocity contrast near the WHB (160°W) between the eastern and western hemispheres is lower than previous estimates using PKPdf phases sampling the bulk part of each hemisphere.

Keywords: body waves; Earth's inner core; east–west hemispheric variations; anisotropy

1. Introduction

Aspherical structures in the Earth's inner core (IC) are traditionally deduced from body-waves and anomalous splitting of eigenfrequencies of normal-mode observations (Deuss, 2014; Tkalčić, 2015). Recent works have shown that the Green's functions of body waves can be reconstructed from correlations between station pairs that record the diffusive wave fields produced by ambient noise and the coda waves of earthquakes, which provide observations of long-period P-waves that sample the center of the IC for nearby station pairs (Huang et al., 2015; Wang et al., 2015). P-wave velocity anisotropy in the IC is characterized by a fast direction aligned subparallel to the Earth's rotation axis (ERA) and a slower direction in the equatorial plane. However, IC anisotropy varies as a function of depth, with notable differences between hemispheres, as follows: an isotropic layer in the upper IC (UIC) overlies an anisotropic lower IC (LIC) (Song and Xu, 2002); the thickness of the isotropic UIC beneath the eastern hemisphere (EH) is 200–400 km, with weak anisotropy (0.5%) in the LIC (Niu and Wen, 2002); and the isotropic part of the UIC beneath the western hemisphere (WH) appears thinner, extends across a range of 20–250 km, and exhibits stronger anisotropy (2–8%) in the LIC (Tanaka and Hamaguchi, 1997; Creager, 1999; Ouzounis and Creager, 2001; Souriau and Poupinet, 2003; Irving and Deuss, 2011a; 2011b). Near the center of the IC, the direction of slow P-wave velocity appears to shift to 45°–51° from the equatorial plane, whereas the direction of fast P-wave velocity remains aligned along polar paths and also along the equatorial plane (Ishii and Dziewoński, 2002; Sun and Song, 2008b; 2008a; Wang et al., 2015). Contrasts between hemispheres are also seen in isotropic velocity and attenuation structures in the upper 500 km of the IC, with high velocity and high attenuation beneath the EH (Niu and Wen, 2001; Tseng et al., 2001; Wen and Niu, 2002; Yu and Wen, 2006; Cormier, 2007; Monnereau et al., 2010; Waszek and Deuss, 2011; Tanaka, 2012; Attanayake et al., 2014); these features extend to the center of the IC (Lythgoe et al., 2014; Huang et al., 2015). East–west hemispheric boundaries have been defined by the longitude corresponding to the anisotropy boundary, the isotropic velocity boundary, and occasionally contrasts in absolute traveltime residuals (Lythgoe et

al., 2014). The eastern hemispheric boundary (EHB) beneath Africa ranges from 10–60°E, whereas the western hemispheric boundary (WHB) beneath the Pacific ranges from 160°E–151°W (Niu and Wen, 2001; Yu and Wen, 2007; Irving and Deuss, 2011a; Waszek and Deuss, 2011; Waszek et al., 2011; Miller et al., 2013; Irving and Deuss, 2015). Near the center of the IC, the EWB and WHB are defined in the range 40–88°E and 95–99°W, respectively (Lythgoe et al., 2014; Huang et al., 2015).

A well-defined hemispheric boundary (HB) is important for two reasons. First, the HB geometry could be used to refine the lateral boundary conditions used in modeling IC dynamics (Deguen, 2012). Second, a precise HB could be used as a marker to track the motions of the IC and to estimate its rotation or oscillation rate (Souriau and Poupinet, 2000; Collier and Helffrich, 2001; Zhang et al., 2005; Waszek et al., 2011; Tkalčić et al., 2013; Yu, 2016). Waszek et al. (2011) and Waszek and Deuss (2011) previously analyzed a large dataset of PKiKP–PKPdf differential traveltime residuals to define the HB in the uppermost IC. However, a high positive PKiKP–PKPdf differential time with PKPdf taking polar paths could be interpreted as an effect of either a high isotropic velocity EH or an anisotropic WH in the uppermost IC; this choice of interpretation directly impacts the inferred location of the HB. Presumably because previous researchers intended to minimize the potential for misinterpretation, polar PKiKP–PKPdf residuals were excluded from their attempts to resolve the HB. The polar–equatorial differences are visible near 180°W in their data, with overlapping df rays (e.g., fig. 5b of Waszek and Deuss 2011). However, these anomalous polar PKiKP–PKPdf residuals are necessary to define the HB and are useful in discussing anisotropy in the uppermost IC. In this study, we determine the WHB in the shallow part of the IC specifically by analyzing PKPbc–PKPdf (herein denoted PKP(bc–df)) along equatorial paths and the azimuthal dependence of the differential time residuals of PKiKP–PKPdf. We show that the anomalous polar PKiKP–PKPdf residuals extend westward across the range 180–155°W, which indicates anisotropy beneath the WH in the uppermost IC with a WHB located at 180°W in the

southern hemisphere. We find that the placement of the WHB in the southern and northern hemispheres is not located at the same meridian, indicating a kink in the WHB with respect to latitude. We assess both the uncertainties and precision of laterally shifting the WHB on differential time residuals across the longitudinal range sampled by PKPdf. We examine the impact of heterogeneous mantle structures on the PKiKP–PKPdf and PKP(bc–df) differential times using the GyPSuM P-wave tomographic model (Simmons et al., 2010). Finally, we discuss how the derived WHB locations compare with those inferred in previous works.

2. Seismic data and measurements of traveltime residuals

Here, PKIKP (or PKPdf, herein abbreviated as df) denotes a P-wave that propagates through the IC, PKiKP (PKPcd) denotes a P-wave that reflects off the inner core boundary (ICB), and PKPbc (abbreviated bc) is a P-wave that propagates through the bottom of the outer core (OC). The raypaths of df and PKiKP, and df and bc remain close throughout the Earth's mantle (Fig. 1a), and their traveltime differences are primarily sensitive to structures near the ICB and in the UIC. PKP waveform data were collected for mb 5.5–6.7 earthquakes from January 1995 to September 2016. The selected PKP data are produced by earthquakes that occurred in the circum-Pacific, toward the Sunda subduction zone (Fig. S1). A total of 1045 PKiKP–PKPdf and 4328 PKP(bc–df) waveforms were selected, with df sampled across the longitude range 155°E–130°W. Note that the Polenet seismic network (code YT) was deployed across Antarctica from 2008 to 2016 (Wiens et al., 2007). The broad longitudinal transect of the YT network preferentially recorded df waves that sampled the IC over the longitudinal range $160°E < \varphi < 155°W$ along quasi-polar paths (defined by an angle $\xi < 40°$ between df and ERA) for earthquakes that occurred at high latitudes in the north Pacific (Figs. 1b, S1a, and S1b). Some of the observed PKiKP–PKPdf times for df waveforms recorded by the YT network are larger than others along equatorial paths, which we interpret as anisotropy in the uppermost 80 km of the IC. Anisotropy beneath this region has not been documented in recent studies. Note also that most of the selected PKP(bc–df) traveltimes were

from intermediate to deep earthquakes that occurred in subduction zones of the southwest Pacific, recorded by densely deployed seismographs in Europe (Figs. 1c and S1c). These sampling paths were previously used to investigate seismic structures near 180°W in the deeper part of the IC (Souriau and Poupinet, 2000; Collier and Helffrich, 2001; Helffrich et al., 2002; Irving and Deuss, 2015).

We analyze PKiKP–PKPdf traveltime differences in the epicentral distance range Δ = 131°–141° and PKP(bc–df) in the range Δ = 146.7°–152°. All waveform data are convolved with a zero-phase two-pole Butterworth bandpass filter with corner frequencies of 0.5 Hz and 2.0 Hz. We manually pick the maximum amplitudes of the df, bc, and PKiKP pulses, and select a 3.00 s time window centered on each pick for time-domain cross-correlation, in which the time series are interpolated to a higher sampling interval of 10 milliseconds. Differential traveltime residuals are the observed differential times of PKiKP–PKPdf and PKP(bc–df) subtracted from values predicted by the AK135 model (Kennett et al., 1995), denoted by *dt*(*PKiKP–PKPdf*) and *dt*(*bc–df*), respectively. Differential time residuals are corrected for path differences due to Earth's ellipticity (Kennett and Gudmundsson, 1996). *dt*(*bc–df*) values are additionally corrected for the time delay due to mantle heterogeneities using the GyPSuM P-wave tomographic model (Simmons et al., 2010) to lessen the impact of regional-scale lower mantle structures on *dt*.

3. Observed PKiKP–PKPdf traveltime residuals

Along equatorial paths ($\xi \geq 40°$) where *dt*(*PKiKP–PKPdf*) times are insensitive to anisotropy in the uppermost IC, *dt*(*PKiKP–PKPdf*) times fall mainly within ±0.30 s when df samples the IC in the range 160°E–170°W. Farther west of 167.5°W, *dt*(*PKiKP–PKPdf*) times become predominantly negative (means and 1σ uncertainties listed in Table 1). Positive *dt* times are interpreted as the result of a faster UIC than the AK135 model predicts. The small *dt*(*PKiKP–PKPdf*) values of ±0.30 s in the EH indicate that the uppermost IC structures predicted by AK135

resemble the EH reasonably well. Since the WH is characterized by a slower isotropic velocity in contrast to the faster EH in the UIC, therefore, we suggest that the transition of the WHB could be suitably placed at 170–160°W (WHB drawn at 160°W in Figs. 1b and 2a), consistent with previous estimates of 173–160°W (Waszek et al., 2011).

Along quasi-polar paths ($\xi < 40°$) where *dt*(*PKiKP–PKPdf*) times reflect anisotropy in the uppermost IC, *dt*(*PKiKP–PKPdf*) values exhibit a laterally increasing trend from 160°E to 155°W. The residuals of the phases that trace polar raypaths from 160 to 175°E are slightly larger than those of phases that trace equatorial raypaths. This suggests that the uppermost IC across 160–175°E is nearly isotropic. Farther westward, from 175°E to 155°W, the magnitude of the polar *dt*(*PKiKP–PKPdf*) increases with increasing distance west, from +0.46 s to +1.67 s, and becomes larger than most equatorial *dt*(*PKiKP–PKPdf*) values for df that sample the EH and WH (Figs. 1b and 2a and Table 1). Such longitudinally dependent polar *dt*(*PKiKP–PKPdf*) values are also clearly visible in the observed waveforms. In Fig. 3, traces 1–3 are PKiKP–PKPdf that sample the IC near 180°W at similar distances; and traces 4–7 and 8–10 are PKiKP–PKPdf that sample the IC from 175–170°W and 168–144°W, respectively. Several polar *dt*(*PKiKP–PKPdf*) that sample from 175°W–155°W are >0.50 s, even at $\Delta < 137°$ (i.e., sampling only the uppermost 50 km of the IC). One argument that supports our interpretation of anisotropy in the uppermost IC is that in some regions near 10°S, 175–160°W, and 20–40°N, 180–155°W, there exist crossing df rays aligned in both the equatorial and polar directions (Fig. 1b). To delineate anisotropy in the IC, we can use the formulation of Sun and Song (2008b):

$$\frac{\delta V}{V} = \alpha + \varepsilon \cos^2 \xi + \gamma \sin^2 2\xi \ , \qquad (1)$$

where α is the velocity perturbation in the equatorial plane, ε is the perturbation in the polar direction, and γ contributes to anisotropy at intermediate angles. From Equation (1), we derived anisotropy by fitting the trend of *dt*(*PKiKP–PKPdf*) as a function of ξ (Fig. 4). For the region spanning 180–155°W, best-fitting α, ε, and γ values of −0.13, 1.75, and −0.95, respectively, were

obtained (Fig. 4a). For the region spanning 160°E–180°W, best-fitting α, ε, and γ values of −0.04, 0.25, and −0.08, respectively, were obtained (Fig. 4b). These best-fitting parameters from Equation (1) yield 1σ uncertainties of 0.14 s and 0.28 s for the regions spanning 160°E–180°W and 180–155°W, respectively. The ε values indicate anisotropy of 1.75% and 0.25% for the regions 180–155°W and 160°E–180°W in the uppermost 80 km of the IC, respectively. Based on *a priori* knowledge of an anisotropic WH and an isotropic EH, we thus infer the region of 180–155°W to be the WH; the WHB could be reasonably placed at 175°E–180°W (WHB drawn at 180°W in Figs. 1b and 2a). The lateral transition from isotropic EH to anisotropic WH is very sharp, occurring over a range of 5°–10° in the uppermost IC. Note that placing of the WHB at 170°W could minimize the uncertainties of the polar *dt*(*PKiKP–PKPdf*) whose df sampling extends across the east–west inter-hemispheres in the northern hemisphere (see the following section). Such a shift of the WHB from 180 to 170°W has a negligible influence on our inferred values of anisotropy for the EH and WH, because the sparse polar PKiKP–PKPdf sampling in the northern hemisphere and those *dt*(*PKiKP–PKPdf*) times with values >1.00 s arise from df turning longitudes located farther west (160–155°W) of the WHB zone (Fig. 1b).

4. Observed PKP(bc–df) traveltime residuals

Observed *dt*(*bc–df*) values are scattered for df sampling along equatorial paths. We first position the WHB at 160°W, derived from *dt*(*PKiKP–PKPdf*) for df phases sampling along equatorial paths. *dt*(*bc–df*) values display a weak lateral gradient of 0.002 s/°, decreasing westward from 155°E to 160°W of the EH. Farther westward, from 160°W to 130°W of the WH, the westward-decreasing lateral gradient steepens to 0.012 s/° (green dotted lines in Fig. 2b). An assessment of the suitable placement of the WHB over a range of longitudes is presented in the next section.

5. Further assessment of the location and uncertainties of the WHB

5.1 Treatment for PKPdf rays traversing the east–west inter-hemispheres of the IC

We inferred the initial location of the WHB using the AK135 one-dimensional (1-D) reference velocity model. However, since the effect of df sampling the east–west (EW) inter-hemispheres of the IC cannot be treated with a 1-D velocity model, this may yield unquantifiable uncertainties for the determined WHB. One recent study considered the effect of df traversing through the EW inter-hemispheres when inverting for isotropic velocity and anisotropy of the IC beneath the north Pacific (Irving and Deuss, 2015), where the df ray was divided into down- and up-going rays and different velocity structures were allowed for the two segments of the df ray to invert for the structures across the WHB of the IC. Here we take a different approach to account for the effect of df traversing the EW inter-hemispheres of the IC. We first derive two 1-D isotropic velocity models, mE2 and mW2, for the EH and WH in the upper 300 km of the IC, respectively, by determining the best-fitting equatorial *dt*(*PKiKP–PKPdf*) and *dt*(*bc–df*) times as a function of distance Δ. For a given WHB position, we compute the length and percentage of the df ray confined in the EH and WH. The df traveltimes in the EH and WH of the IC are proportional to the percentage of df ray length traveling in the EH and WH, which are computed from mE2 and mW2, respectively. The differential time residuals of PKiKP–PKPdf and PKP(bc–df) are thus based on mE2 and mW2. By shifting the position of the WHB from 170°E to 140°W, we examine how the means and root-mean-square (RMS) residuals of *dt*(*PKiKP–PKPdf*) and *dt*(*bc–df*) vary with WHB position for longitudinal bins spanning 155°E–130°W. The optimal position of the WHB is then inferred from the observed minima in the means and RMS residuals across the range of longitudinal bins.

5.2 Derivation of 1-D velocity models for the eastern and western hemispheres of the IC

Previous seismic studies have inferred velocity models for the EH and WH of the IC (Wen and Niu, 2002; Yu and Wen, 2006; Sun and Song, 2008b; Cormier et al., 2011; Irving and Deuss, 2011a; Waszek and Deuss, 2011; Tanaka, 2012; Attanayake et al., 2014). The 1-D velocity models

E1 and W2 for the EH and WH, respectively, derived from Yu and Wen (2006), were used in the present study. We use E1 and W2 as starting IC models for the two hemispheres to fit *dt*(*PKiKP–PKPdf*) and *dt*(*bc–df*). It is noted that the E1 and W2 models have subtle differences in P-wave velocity structures in the lowermost OC (Yu et al., 2005). However, such a difference in velocity in the lowermost OC between the two hemispheres may not be seismically resolvable due to the scatter in the observed differential time data (Cormier et al., 2011). Since our goal here is to investigate the position of the WHB of the IC, the OC is assumed to have identical baseline structures between the two hemispheres, to avoid complicated interpretations. Although the two derived 1-D velocity models for the EH and WH of the IC may be non-unique, we emphasize that our aim is to use the mE2 and mW2 modified isotropic velocity models to approximate the df times propagating through the EH and WH, and to take into account the effect of the df rays traversing the EW inter-hemispheres of the IC. E1 yields slightly faster times to account for the observed *dt*(*PKiKP–PKPdf*), but the modeled times are too fast to account for *dt*(*bc–df*) of the EH along equatorial paths by 0.3 s, whereas W2 yields slightly slower times to explain *dt*(*PKiKP–PKPdf*) and *dt*(*bc–df*) for df rays sampling the WH (Figs. S2a and S2c). Since the velocity gradient in the lowermost OC of W2 is similar to that of AK135, we adopt the mantle and OC structures of W2 and modify the velocity models of the IC for the EH and WH, producing our mE2 and mW2 models. For the mE2 model, we reduce the velocity step across the ICB, extending the same velocity gradient of E1 to the deeper part of the IC. The mE2 model can efficiently lower the model-predicted *dt*(*bc–df*) to fit the means of observations over Δ = 147°–152°, and also reasonably account for *dt*(*PKiKP–PKPdf*) over Δ = 131°–135°, but it still slightly over-predicts observations over Δ = 136°–141°. Velocity structures in the uppermost IC, decreased to fit *dt*(*PKiKP–PKPdf*) of the EH over Δ = 136°–141°, will be expected to produce even smaller *dt*(*bc–df*), and thus increase the misfit to the observed *dt*(*bc–df*). For the WH, the mW2 model has a slightly higher velocity step across the ICB and maintains the same velocity gradient of W2 in the upper 300 km of the IC, which fits *dt*(*PKiKP–PKPdf*) and *dt*(*bc–df*) values reasonably well (Figs. S2a, S2c, and S2d). Note

that mE2 and mW2 still under-predict the polar *dt*(*PKiKP–PKPdf*) of the EH and WH to different degrees (Fig. S2b).

5.3 Precision and uncertainties of the determined WHB

We examine the sensitivity and uncertainties of the laterally varying WHB on *dt*(*PKiKP–PKPdf*) along equatorial and polar paths (Figs. 5 and 6). For *dt*(*PKiKP–PKPdf*) along equatorial paths and over longitudinal bins spanning 170°E–160°W, the westward shift of the WHB from 170°E to 160°W could progressively lower *dt*(*PKiKP–PKPdf*) values and their respective means (Figs. 5a–5d). In the case of the WHB positioned at 170°E, the regions westward of 170°E would be attributed to the WH (Fig. 5a). Because df rays propagating through this region would have modeled times based on the slower mW2 model, positive *dt*(*PKiKP–PKPdf*) times are observed for the longitudinal bins spanning 170°E–160°W (Fig. 5a). For the WHB positioned at either 170°W or 160°W, means of *dt*(*PKiKP–PKPdf*) relative to the model-predicted times fluctuate around zero over broad longitudinal bins, indicating that the mE2 and mW2 models perform reasonably well in approximating the df time traversing the EH, WH, and EW inter-hemispheres (Figs. 5c and 5d). Placing the WHB westward at 150°W and 140°W yields negative values for most *dt*(*PKiKP–PKPdf*) and their means over longitudinal bins spanning 170–140°W, because mE2 is too fast for *dt*(*PKiKP–PKPdf*), whose df rays are turning through this part of the defined 'EH' (Figs. 5e and 5f). Figs. 5g and 5h display the means and RMS residuals of *dt*(*PKiKP–PKPdf*) relative to the modeled values for the westward shift of the WHB from 170°E to 140°W. Means and RMS residuals of *dt*(*PKiKP–PKPdf*) calculated within a 10° longitudinal bin for each position of the WHB are plotted side by side as different colors. Previously discussed scenarios for variations in the means of *dt*(*PKiKP–PKPdf*) corresponding to the shift of the WHB from 170°E to 140°W are illustrated by the bars in the longitudinal bins in Fig. 5g. When the WHB is positioned at 170–160°W, minimum means and RMS residuals of *dt*(*PKiKP–PKPdf*) are often observed over the same longitudinal bins (red and light blue bars in Figs. 5g and 5h). Thus, the optimal position of the

WHB would be 170–160°W to account for *dt*(*PKiKP–PKPdf*) whose df sampling the EH are separated from the WH along equatorial paths, which is consistent with our earlier inferences.

A lateral increase is observed in both the means and RMS residuals of the polar *dt*(*PKiKP–PKPdf*) calculated relative to the modeled times across 180°W (Figs. 6g and 6h). While shifting the WHB farther westward could lower the means and RMS residuals over certain longitudinal bins, those values are still notably larger than those over the region spanning 160°E–180°W. For instance, placing the WHB at 160°W would produce lower means and RMS residuals over 180–170°W compared with those at 180°W, but the means of polar *dt* are still larger than those over 160°E–180°W by 0.4–0.6 s, producing the strong contrast in means and RMS residuals of *dt* between 160°E–180°W and 180–160°W within the defined 'EH' (Fig. 6d, and red bars in Figs. 6g and 6h). Our uncertainty analysis of the polar *dt*(*PKiKP–PKPdf*) due to laterally shifting the WHB suggests that placing the WHB at 180°W is optimal to distinguish the observed *dt*(*PKiKP–PKPdf*) for df sampling the isotropic EH from the anisotropic WH, which is consistent with our earlier inferences.

For the equatorial *dt*(*bc–df*), shifting the WHB across the 180–140°W region is examined through analysis of the means and RMS residuals of *dt*(*bc–df*) over longitudinal bins spanning 155°E–130°W (Fig. S3). With the exception of placing the WHB at 180°W, which produces a larger RMS residual over 180–170°W (gray bars in Fig. S3g), the RMS residuals are not diagnostic enough to examine the effect of the WHB on *dt*(*bc–df*) over 180–160°W (Fig. S3g). However, placing the WHB at 170–160°W produces slight minimum means over bins spanning 180–160°W (red and light blue bars in Fig. S3f). The position of the WHB at depth could be placed at 160°W, but this is less definitive due to scattered PKP(bc–df).

6. Discussion

6.1 Mantle effects

The Fresnel zone is ~150 km in the lowermost mantle for PKP waves at 1 Hz. For the PKiKP–PKPdf phases, the two rays are separated by ~50 km at the core–mantle boundary (CMB), and the Fresnel zones of these two phases overlap (e.g., fig. 12 of Yu and Wen 2007). Seismic heterogeneities near the CMB should thus have a negligible influence on observed *dt*(*PKiKP–PKPdf*). We examine the mantle effects on *dt*(*PKiKP–PKPdf*) using the GyPSuM P-wave tomographic model, and observe that mantle structures within the GyPSuM model produce null effects on *dt*(*PKiKP–PKPdf*) (Fig. S4a). For the PKP(bc–df) phases, the separations of the two rays are ~300 km (~5°) at the CMB, approximately double the size of the Fresnel zone. Any isolated low-velocity structures with wavelengths of 3°–5° at the CMB could influence only the bc or df ray. In this scenario, both positive (exclusively delaying bc) and negative (delaying df) *dt*(*bc–df*) would be observed over short distances. Across the region spanning 155°E–180°W, the GyPSuM model predicted *dt*(*bc–df*) values range from –0.2 s to +0.5 s, and also exhibit a westward-decreasing trend. Farther westward of 170°W, the majority of the predicted *dt*(*bc–df*) values are within ±0.2 s (Fig. S4b). *dt*(*bc–df*) relative to the reference velocity model AK135, without time shift corrections due to heterogeneous mantle structures of the GyPSuM model, yield a slightly steeper westward-decreasing gradient of 0.005 s/° (not shown) when compared with *dt*(*bc–df*) relative to AK135 with the time shift corrections of the GyPSuM model, which yields a lateral gradient of 0.002 s/° (Fig. 2b). Regional-scale structures in the lowermost mantle have a potential influence on *dt*(*bc–df*), and could mask or distort signals arising from the IC structures.

6.2 Latitudinal dependence of the WHB

There are discrepancies in the WHB longitude estimates derived from equatorial and polar *dt*(*PKiKP–PKPdf*) data, and placing the WHB at either 170–160°W or 180°W conflicts with a subset of observations of the known behaviors of the EH and WH. One explanation is a 10°–20° transition zone where UIC anisotropy increases rapidly with distance from 180 to 170–160°W.

Alternatively, one could invoke a kink in the WHB to account for *dt*(*PKiKP–PKPdf*) observations whose df sample different locations in the southern and northern hemispheres. We assess the uncertainties associated with a lateral shift of the WHB on *dt*(*PKiKP–PKPdf*) for which df samples the northern and southern hemispheres, as carried out previously and shown in Figs. 5, 6, and S3. We first place a north–south division at 8°N. The equatorial and polar *dt*(*PKiKP–PKPdf*) are examined to determine their uncertainties associated with laterally shifting the WHB, which is dependent on the resultant df sampling through the northern (8–90°N) and southern (90°S–8°N) hemispheres. However, it should be noted that the uneven sampling coverage in the northern hemisphere means that the majority of the observed *dt*(*PKiKP–PKPdf*) are governed predominantly by rays along equatorial paths (Fig. S5a), whereas in the southern hemisphere, the majority of the *dt*(*PKiKP–PKPdf*) data arise from df sampling along polar paths (Fig. S5d). For the equatorial PKiKP–PKPdf whose df sample the northern hemisphere, placing the WHB at 160°W produces minimal means and RMS residuals over 180–160°W (red bars in Figs. 7a and 7b). For the equatorial *dt*(*PKiKP–PKPdf*) whose df sample the southern hemisphere, the WHB at 180–170°W appears to generate minimal means over bins 180–160°W (gray and light blue bars in Fig. 7c). For the polar *dt*(*PKiKP–PKPdf*), the means and RMS residuals exhibit a lateral increase at 170°W and 180°W for the northern and southern hemispheres, respectively (Fig. 8). Our assessment of the uncertainties associated with *dt*(*PKiKP–PKPdf*) for df sampling along equatorial and polar paths suggests a latitudinal dependence of the WHB, with the WHB positioned near 170–160°W in the northern hemisphere and 180°W in the southern hemisphere.

Our inferred latitudinal dependence of the WHB is illustrated in Fig. 9 and listed in Table 2. The WHB can be placed at 175°E–180°W in the southern hemisphere (35°S–8°N). The WHB could deviate slightly eastward from 180°W, 35°S to 175°E, 8°N, to separate the nearly isotropic EH from the moderately anisotropic WH. Two likely scenarios arise when extending the WHB northward from 175°E, 8°N (Figs. 9a and 9b). For the isotropic structures, the WHB first requires a

westward-deviating kink at 160°W, 30°N, followed by a fixed meridian at 160°W in the northern hemisphere (30–90°N), to distinguish the faster EH from the slower WH (yellow solid-black dotted line in Figs. 1b and 9a). The isotropic velocity of the EH is 0.13% faster and the WH is 0.43% slower than that of the AK135 model. Our estimated isotropic velocity contrast is 0.56% between the EH and WH near the WHB (160°W) (Fig. 9a), which is lower than the previous estimates of 1.0%–1.4% for the bulk part of the EH and WH (Wen and Niu, 2002; Waszek and Deuss, 2011). The smaller contrast of the isotropic velocity near the WHB is due to the isotropic velocity of the EH and WH near the WHB is of about 0.27% slower and 0.17% faster than that estimated for the bulk part of the EH and WH, respectively (Figs. 9a and S2d). For the anisotropic structures, the westward-deviating kink in the WHB could be placed at 170°W, 30°N, followed by a fixed meridian at 170°W in the northern hemisphere, to distinguish the nearly isotropic EH from the moderately anisotropic WH, with 0.25% and 1.75% anisotropy for the EH and WH, respectively (Figs. 4 and 9b). Such a WHB with a kink seems *ad hoc* and subjective; however, it could minimize the uncertainties of the observed *dt*(*PKiKP–PKPdf*), as well as reconcile most observed *dt*(*PKiKP–PKPdf*) values with known patterns for the eastern and western hemispheres of the UIC. In the deeper part, the WHB location is less definitive and could remain at 160°W. The isotropic velocities for the EH and WH are 0.049% and 0.043% higher than those in the AK135 model, respectively. Our estimate for the isotropic velocity contrast between the EH and WH near the WHB (160°W) at depth is also lower than the previous estimate of 0.4% for the bulk part of the EH and WH (Fig. 9c) (Yu and Wen, 2006). Our analyses indicate that the WHB is latitude-dependent in the uppermost IC, but depth-independent for isotropic structures in the upper 300 km of the IC.

6.3 Depth-dependent fine structures near the WHB of the IC

It has been suggested that stratified structures in the IC, such as the depth-dependence on attenuation (Li and Cormier, 2002; Yu and Wen, 2006), the isotropic UIC–anisotropic LIC transition (e.g., Niu and Wen, 2002; Irving and Deuss, 2011b; Tkalčić, 2015), the hemispheric

boundary (Waszek et al., 2011), and the regional-scale anomalous layer in the UIC (Stroujkova and Cormier, 2004), reveal sophisticated seismic structures over the depth of the IC. Here we examine the depth-dependence of fine structures over the region spanning 155°E–130°W by plotting *dt*(*PKiKP–PKPdf*) and *dt*(*bc–df*) as a function of df turning depth in the IC (Fig. S5). We also divide our PKiKP–PKPdf data along equatorial and polar paths into df sampling located in the northern and southern hemispheres. Note that the Fresnel zone is 200 km and 300 km in the upper 80 km and 150–300 km of the IC, respectively, for PKPdf waves at 1 Hz. Except for the contrast in *dt*(*PKiKP–PKPdf*) near the WHB, depth-dependent fine structures are obscure in the upper 300 km of the IC.

6.4 Comparisons with previous results

Many previous studies have attempted to map the boundary between the two hemispheres of the IC. Seismic phases analyzed in previous works include PKiKP–PKPdf differential times (Niu and Wen, 2001; Waszek et al., 2011), PKP(bc–df) (Tanaka and Hamaguchi, 1997), and PKP(bc–df) and PKP(ab–df) along polar and equatorial paths (Creager, 1999; Irving and Deuss, 2011a). The exact locations of the WHB vary from an early estimate of 160°E (Creager, 1999) to a recent estimate of 151°W (Irving and Deuss, 2011a). The discrepancies among the inferred WHB values could arise from the sensitivity of PKP differential times, inadequate data, sparse raypath coverage, misinterpretations of polar df traveltimes due to a faster EH or an anisotropic WH, or different reference velocity models. PKP(bc–df) times largely avoid the uncertainties due to large-scale lateral structures in the lowermost mantle, as the latter have a much greater influence on PKPab. Polar PKP(bc–df) times with a confined longitudinal extent allow more precise constraints on the WHB than equatorial PKP(bc–df) times, because equatorial df rays traverse the EW inter-hemispheres at depths of the IC. However, polar PKP(bc–df) sampling near the WHB is often insufficient and uneven, leading to a net uncertainty of 50° in the WHB location (Creager, 1999; Irving and Deuss, 2011a). PKiKP–PKPdf offers an optimal dataset for determining the position of

the WHB, because the short lengths of the df rays in the uppermost IC both lower the effect of EW inter-hemispheres sampled by df, and *dt*(*PKiKP–PKPdf*) are insensitive to the regional-scale structures in the lowermost mantle (Fig. S4a), resulting in more focused *dt*(*PKiKP–PKPdf*) compared with *dt*(*bc–df*). Our inferred WHB in the northern hemisphere, near 170–160°W, is consistent with recent estimates of 173–160°W (Waszek and Deuss, 2011; Waszek et al., 2011). The main difference between these previous studies and this work is that the sampling coverage of the polar PKiKP–PKPdf is improved in the range 180–155°W here, which reveals the sharp lateral isotropy–anisotropy transition and helps place the WHB at 180°W in the southern hemisphere. We also emphasize that positive, laterally varying *dt*(*PKiKP–PKPdf*) values along polar paths reflect variations in anisotropy beneath the Pacific in the uppermost IC, rather than the effects of a high isotropic velocity EH, because the mE2 isotropic model slightly under-predicts those polar *dt*(*PKiKP–PKPdf*) of the EH and considerably under-predicts nearly all polar *dt* over the 180–155°W range of the WH (Figs. S2b and 6).

In fact, an irregular and latitudinally dependent WHB beneath the Pacific has been implied by several recent studies using PKP(bc–df) (Miller et al., 2013; Irving and Deuss, 2015). Irving and Duess (2015) observed *dt*(*bc–df*) with values of +0.5 to +1.5 s using df sampling in the region 15–30°N, 180–150°W along polar paths (their Fig. 2). Because they adopted a straight WHB at 151°W from Irving and Duess (2011a), the region bounded by 180–150°W would correspond to their defined EH. The observed positive *dt*(*bc–df*) values along polar paths imply that the EH is moderately anisotropic at depth within the IC. If we adopt our inferred latitudinal dependence of the WHB, most variations in their PKP(bc–df) in the region 15–30°N, 180–150°W could be attributed to the WH, which is more compatible with other interpretations of anisotropy beneath the WH at depth (Tanaka and Hamaguchi, 1997; Creager, 1999; Deuss, 2014). Hence, our inferred WHB could also partly reconcile the previous interpretations.

In addition, Irving and Deuss (2015) suggested that the hemispheric anisotropic velocity structures beneath the Pacific would be altered with *a priori* knowledge of an anisotropic WH and an isotropic EH once the presence of IC anisotropy is introduced in the inversion, whereas the EW hemispheric isotropic structures are retained using equatorial data in the inversion. These inferences suggest that df times sampling along the polar paths are truly more complex, and detect regional variations more readily than those along equatorial paths. This also indicates that the isotropic hemispheres would not necessarily correspond to the anisotropic hemispheres, leading to the discrepancies in the HB defined using equatorial and polar *dt*(*PKiKP–PKPdf*). As discussed, the uncertainties of the HB in the northern and southern hemispheres are examined separately using both equatorial and polar *dt*(*PKiKP–PKPdf*). Such a discrepancy would yield only 0–10° variations in the position of the HB in the northern and southern hemispheres (Figs. 7 and 8).

6.5 Possible implications

The isotropic part of the uppermost IC has been well established in previous studies. The isotropic layer is thinner and exhibits regional variations elsewhere beneath the WH (Deuss, 2014; Tkalčić, 2015). Our inferred 1.75% anisotropy beneath the Pacific, across 180–150°W, in the uppermost IC is new, and has several implications. First, the splitting functions of normal-mode observations are most sensitive to UIC structure and thus indicate anisotropy there, in contrast to the isotropic UIC previously inferred from body-wave observations (Deuss, 2014). Since this study suggests anisotropy beneath the Pacific across 180–150°W in the UIC, our findings are the first that could reconcile normal-mode and body-wave UIC observations. In addition, solidification texturing of the IC due to heat extraction caused by cylindrical OC convection would imply anisotropy of the UIC (Bergman, 1997; Deguen, 2012), and our observations are partly compatible with a model for IC growth by solidification texturing. However, regional variations in polar *dt*(*PKiKP–PKPdf*) near 180°W could also imply an isotropic UIC and a laterally varying anisotropic LIC. It remains to be

confirmed how anisotropy in the uppermost IC evolves as a function of depth and anisotropy elsewhere in the uppermost IC in the WH. This will be the subject of forthcoming studies.

Several dynamic models have been proposed to account for hemispheric structures in the UIC. One model imposes longstanding thermo-chemical structures in the lower mantle that couple OC convection and influence regional IC growth rate (Aubert et al., 2008). Though it is not explicitly stated in that study, it would be expected that such thermo-chemical structures in the lower mantle would generate a broad, smooth east–west transition in the IC. Alternately, if invoking mechanisms from the IC internally, several proposed dynamic models are able to reproduce hemispheric differences in the IC (Alboussière et al., 2010; Monnereau et al., 2010; Deguen, 2012; Aubert et al., 2013). If the temperature profile of the IC is superadiabatic, an unstable eastward translational convection would occur, resulting in melting in the EH and solidification in the WH. A proposed model of a convectively translating IC produced a smooth transition between the two hemispheres, but a subsequent study revealed that this translation could produce a fairly sharp HB (Geballe et al., 2013). However, this model would require rather sophisticated solidification processes, in addition to convective translation, to account for the presence of isotropy and anisotropy, and latitudinally dependent hemispheric boundary in the uppermost IC.

7. Conclusions

This study determined the western side of the east–west hemispheric boundary near 180°W in the inner core, using differential time residuals of PKiKP–PKPdf and PKP(bc–df) whose PKPdf sample the region 155°E–130°W. The western hemisphere of the inner core is well known for its thin isotropic layer overlying strong anisotropy at depth, low isotropic velocity, and low attenuation, in contrast to the eastern hemisphere. The hemispheric boundary could thus be determined by searching for the meridian at which the transition of the contrast in anisotropy or isotropic velocity

is clearest. Differential time residuals of PKiKP–PKPdf, computed relative to the AK135 model, reveal that the hemispheric boundary could be placed at 175°E–180°W in the southern hemisphere to distinguish the nearly isotropic (0.25%) eastern hemisphere from the moderately anisotropic (1.75%) western hemisphere; the hemispheric boundary is placed at 170–160°W in the northern hemisphere to separate the faster eastern hemisphere from the slower western hemisphere. These interpretations imply either a 10°–20° sharp gradient in the degree of anisotropy or a 10°–20° kink and latitudinally-dependent hemispheric boundary in the uppermost inner core. The isotropic velocity contrast is 0.56% between the eastern and western hemispheres near the western hemisphere boundary (160°W) in the uppermost 80 km of the inner core, lower than previous estimates using PKiKP–PKPdf sampling the bulk part of each hemisphere. Differential time residuals of PKP(bc–df) are more scattered, exhibiting two westward-decreasing gradients, with 0.002 s/° observed across 155°E–160°W of the eastern hemisphere and a steeper gradient of 0.012 s/° observed across 160°W–130°W of the western hemisphere. The hemispheric boundary could remain at 160°W in the deeper part of the inner core, but this estimate is less definitive. We assess the uncertainty and precision of the laterally shifting hemispheric boundary on differential time residuals of PKiKP–PKPdf and PKP(bc–df) relative to the composite models for the eastern and western hemispheres of the inner core. Consistent values of the inferred hemispheric boundary and its latitudinal dependence are observed by taking into account the effect of PKPdf propagating through the east–west inter-hemispheres of the inner core. We also examine the depth-dependence of the hemispheric boundary and fine structures near the western hemisphere boundary in the upper 300 km of the inner core, but this pattern is obscure. The impact of heterogeneous mantle structures on PKP differential times is examined using the GyPSuM model, which have null influence on differential times of PKiKP–PKPdf, but localized structures in the lowermost mantle may have potential impacts on the PKP(bc–df) differential times and could be responsible for the scattered PKP(bc–df) observations. Our inferred latitudinally dependent hemispheric boundary can partly reconcile previous interpretations of anisotropy detected beneath the eastern hemisphere at depth.

Lateral variations in the transition from isotropy to anisotropy and the latitudinally dependent hemispheric boundary near 180°W suggest sophisticated dynamics operating in the inner core, leading to inner core regional growth/melting with complex textures as a result.

Acknowledgements and Data

Waveform data were assembled from the following seismic networks: AC, AI, AU, BE, BL, BN, BS, CA, CH, CI, CM, CN, CZ, DK, EE, EI, ER, FN, FR, G, GB, GE, GR, GT, GU, HE, HF, HT, HU, IC, II, IU, IV, KO, MN, MT, NI, NL, NO, NU, OE, PL, PM, RD, RO, SI, SJ, SK, SL, SX, TH, TU, UP, US, XE, XP, XR, YI, YO, and YT. Data were downloaded from the following data centers: IRIS-DMC, ORFEUS, GFZ Potsdam, SZGRF, RESIF, INFP, INGV, SED, and CNSN. We acknowledge constructive reviews from two reviewers and suggestions by the Editor, Vernon Cormier, which particularly helped to strengthen the uncertainty analyses regarding the placement of the hemispheric boundary and improve the overall presentation of the manuscript.

Funding sources

This study was supported by the Institute of Earth Sciences, Academia Sinica, and by grants MOST-105-2116-M-001-011- and MOST-106-2116-M-001-009- from the Ministry of Science and Technology, Taiwan. The funding sponsors did not interfere with, and did not contribute to, the study design, analysis, interpretation, and decision to submit this study for publication.

Competing interests

The authors have no competing interests to declare.

References

Alboussière, T., Deguen, R., Melzani, M., 2010. Melting-induced stratification above the Earth's inner core due to convective translation. Nature 466, 744–747, http://dx.doi.org/10.1038/nature09257.

Attanayake, J., Cormier, V.F., de Silva, S.M., 2014. Uppermost inner core seismic structure – new insights from body waveform inversion. Earth Planet. Sci. Lett. 385, 49–58, http://dx.doi.org/10.1016/j.epsl.2013.10.025.

Aubert, J., Amit, H., Hulot, G., Olson, P., 2008. Thermochemical flows couple the Earth's inner core growth to mantle heterogeneity. Nature 454, 758–761, http://dx.doi.org/10.1038/nature07109.

Aubert, J., Finlay, C.C., Fournier, A., 2013. Bottom-up control of geomagnetic secular variation by the Earth's inner core. Nature 502, 219–223, http://dx.doi.org/10.1038/nature12574.

Bergman, M.I., 1997. Measurements of elastic anisotropy due to solidification texturing and the implications for the Earth's inner core. Nature 389, 60–63.

Collier, J.D., Helffrich, G., 2001. Estimate of inner core rotation rate from United Kingdom regional seismic network data and consequences for inner core dynamical behaviour. Earth Planet. Sci. Lett. 193, 3–4, 523–537, http://dx.doi.org/10.1016/S0012-821X(01)00520-9.

Cormier, V.F., 2007. Texture of the uppermost inner core from forward- and back-scattered seismic waves. Earth Planet. Sci. Lett. 258, 3–4, 442–453, http://dx.doi.org/10.1016/j.epsl.2007.04.003.

Cormier, V.F., Attanayake, J., He, K., 2011. Inner core freezing and melting: Constraints from seismic body waves. Phys. Earth Planet. Inter. 188, 3–4, 163–172, http://dx.doi.org/10.1016/j.pepi.2011.07.007.

Creager, K.C., 1999. Large-scale variations in inner core anisotropy. J. Geophys. Res. 104, B10, 23127–23139.

Deguen, R., 2012. Structure and dynamics of Earth's inner core. Earth Planet. Sci. Lett. 333–334, 211–225, http://dx.doi.org/10.1016/j.epsl.2012.04.038.

Deuss, A., 2014. Heterogeneity and anisotropy of Earth's inner core. Annu. Rev. Earth Planet. Sci. 42, 103–126, http://dx.doi.org/10.1146/annurev-earth-060313-054658.

Geballe, Z.M., Lasbleis, M., Cormier, V.F., Day, E.A., 2013. Sharp hemisphere boundaries in a translating inner core. Geophys. Res. Lett. 40, 1719–1723, http://dx.doi.org/10.1002/grl.50372.

Helffrich, G., Kaneshima, S., Kendall, J.M., 2002. A local, crossing-path study of attenuation and anisotropy of the inner core. Geophys. Res. Lett. 29, 12, 1568, http://dx.doi.org/10.1029/2001GL014059.

Huang, H.H., Lin, F.C., Tsai, V.C., Koper, K.D., 2015. High-resolution probing of inner core structure with seismic interferometry. Geophys. Res. Lett. 42, 10622–10630, http://dx.doi.org/10.1002/2015GL066390.

Irving, J.C.E., Deuss, A., 2011a. Hemispherical structure in inner core velocity anisotropy. J. Geophys. Res. 116, B04307, http://dx.doi.org/10.1029/2010JB007942.

Irving, J.C.E., Deuss, A., 2011b. Stratified anisotropic structure at the top of Earth's inner core: A normal mode study. Phys. Earth Planet. Inter. 186, 59–69, http://dx.doi.org/10.1016/j.pepi.2011.03.003.

Irving, J.C.E., Deuss, A., 2015. Regional seismic variations in the inner core under the North Pacific. Geophys. J. Int. 203, 3, 2189–2199, http://dx.doi.org/10.1093/gji/ggv435.

Ishii, M., Dziewoński, A.M., 2002. The innermost inner core of the earth: Evidence for a change in anisotropic behavior at the radius of about 300 km. Proc. Nat. Acad. Sci. 99, 22, 14026–14030, http://dx.doi.org/10.1073/pnas.172508499.

Kennett, B.L.N., Engdahl, E.R., Buland, R., 1995. Constraints on seismic velocities in the Earth from traveltimes. Geophys. J. Int. 122, 1, 108–124, http://dx.doi.org/10.1111/j.1365-246X.1995.tb03540.x.

Kennett, B.L.N., Gudmundsson, O., 1996. Ellipticity corrections for seismic phases. Geophys. J. Int. 127, 1, 40–48, http://dx.doi.org/10.1111/j.1365-246X.1996.tb01533.x.

Li, X., Cormier, V.F., 2002. Frequency-dependent seismic attenuation in the inner core 1. A viscoelastic interpretation. J. Geophys. Res. 107, B12, 2361, http://dx.doi.org/10.1029/2002JB001795.

Lythgoe, K.H., Deuss, A., Rudge, J.F., Neufeld, J.A., 2014. Earth's inner core: Innermost inner core or hemispherical variations? Earth Planet. Sci. Lett. 385, 181–189, http://dx.doi.org/10.1016/j.epsl.2013.10.049.

Miller, M.S., Niu, F., Vanacore, E.A., 2013. Aspherical structural heterogeneity within the uppermost inner core: Insights into the hemispherical boundaries and core formation. Phys. Earth Planet. Inter. 223, 8–20, http://dx.doi.org/10.1016/j.pepi.2013.02.001.

Monnereau, M., Calvet, M., Margerin, L., Souriau, A., 2010. Lopsided growth of Earth's inner core. Science 328, 1014–1017, http://dx.doi.org/10.1126/science.1186212.

Niu, F., Wen, L., 2001. Hemispherical variations in seismic velocity at the top of the Earth's inner core. Nature 410, 1081–1084.

Niu, F., Wen, L., 2002. Seismic anisotropy in the top 400 km of the inner core beneath the "eastern" hemisphere. Geophys. Res. Lett. 29, 12, 1611, http://dx.doi.org/10.1029/2001GL014118.

Ouzounis, A., Creager, K.C., 2001. Isotropy overlying anisotropy at the top of the inner core. Geophys. Res. Lett. 28, 22, 4331–4334, http://dx.doi.org/10.1029/2001GL013341.

Simmons, N.A., Forte, A.M., Boschi, L., Grand, S.P., 2010. GyPSuM: A joint tomographic model of mantle density and seismic wave speeds. J. Geophys. Res. 115, B12310, http://dx.doi.org/10.1029/2010JB007631.

Song, X., Xu, X., 2002. Inner core transition zone and anomalous PKP(DF) waveforms from polar paths. Geophys. Res. Lett. 29, 4, 1042, http://dx.doi.org/10.1029/2001GL013822.

Souriau, A., Poupinet, G., 2000. Inner core rotation: a test at the worldwide scale. Phys. Earth Planet. Inter. 118, 1–2, 13–27, http://dx.doi.org/10.1016/S0031-9201(99)00131-4.

Souriau, A., Poupinet, G. (2003). Inner core rotation: A critical appraisal, in *Earth's Core Dynamics, Structure, Rotation*, 65–82, eds, Dehant, V., Creager, K. C., Karato, S. & Zatman, S., American Geophysical Union, Washington D.C.

Stroujkova, A., Cormier, V.F., 2004. Regional variations in the uppermost 100 km of the Earth's inner core. J. Geophys. Res. 109, B10307, http://dx.doi.org/10.1029/2004JB002976.

Sun, X., Song, X., 2008a. The inner inner core of the Earth: Texturing of iron crystals from three-dimensional seismic anisotropy. Earth Planet. Sci. Lett. 269, 56–65, http://dx.doi.org/10.1016/j.epsl.2008.01.049.

Sun, X., Song, X., 2008b. Tomographic inversion for three-dimensional anisotropy of Earth's inner core. Phys. Earth Planet. Inter. 167, 1–2, 53–70, http://dx.doi.org/10.1016/j.pepi.2008.02.011.

Tanaka, S., Hamaguchi, H., 1997. Degree one heterogeneity and hemispherical variation of anisotropy in the inner core from PKP(BC)–PKP(DF) times. J. Geophys. Res. 102, B2, 2925–2938.

Tanaka, S., 2012. Depth extent of hemispherical inner core from PKP(DF) and PKP(Cdiff) for equatorial paths. Phys. Earth Planet. Inter. 210–211, 50–62, http://dx.doi.org/10.1016/j.pepi.2012.08.001.

Tkalčić, H., Young, M., Bodin, T., Ngo, S., Sambridge, M., 2013. The shuffling rotation of the Earth's inner core revealed by earthquake doublets. Nat. Geosci. 6, 497–502, http://dx.doi.org/10.1038/NGEO1813.

Tkalčić, H., 2015. Complex inner core of the Earth: The last frontier of global seismology. Rev. Geophys. 53, 1, 59–94, http://dx.doi.org/10.1002/2014RG000469.

Tseng, T.L., Huang, B.S., Chin, B.H., 2001. Depth-dependent attenuation in the uppermost inner core from the Taiwan short period seismic array PKP data. Geophys. Res. Lett. 28, 3, 459–462, http://dx.doi.org/10.1029/2000GL012118.

Wang, T., Song, X., Xia, H.H., 2015. Equatorial anisotropy in the inner part of Earth's inner core from autocorrelation of earthquake coda. Nat. Geosci. 8, 3, 224–227, http://dx.doi.org/10.1038/NGEO2354.

Waszek, L., Deuss, A., 2011. Distinct layering in the hemispherical seismic velocity structure of Earth's upper inner core. J. Geophys. Res. 116, B12313, http://dx.doi.org/10.1029/2011JB008650.

Waszek, L., Irving, J., Deuss, A., 2011. Reconciling the hemispherical structure of Earth's inner core with its super-rotation. Nat. Geosci. 4, 264–267, http://dx.doi.org/10.1038/NGEO1083.

Wen, L., Niu, F., 2002. Seismic velocity and attenuation structures in the top of the Earth's inner core. J. Geophys. Res. 107, (B11), 2273, http://dx.doi.org/10.1029/2001JB000170.

Wiens, D.A., Nyblade, A., Aster, R.C. (2007). IPY POLENET-Antarctica: Investigating links between geodynamics and ice sheets International Federation of Digital Seismograph Networks. Other/Seismic Network.

Yu, W., Wen, L., Niu, F., 2005. Seismic velocity structure in the Earth's outer core. J. Geophys. Res. 110, B02302, http://dx.doi.org/10.1029/2003JB002928.

Yu, W., Wen, L., 2006. Seismic velocity and attenuation structures in the top 400 km of the Earth's inner core along equatorial paths. J. Geophys. Res. 111, B07308, http://dx.doi.org/10.1029/2005JB003995.

Yu, W., Wen, L., 2007. Complex seismic anisotropy in the top of the Earth's inner core beneath Africa. J. Geophys. Res. 112, B08304, http://dx.doi.org/10.1029/2006JB004868.

Yu, W., 2016. Time-dependent inner core structures examined using repeating earthquakes in subduction zones of the southwest Pacific. Geophys. J. Int. 204, 1204–1215, http://dx.doi.org/10.1093/gji/ggv508.

Zhang, J., Song, X., Li, Y., Richards, P.G., Sun, X., Waldhauser, F., 2005. Inner core differential motion confirmed by earthquake waveform doublets. Science 309, 1357–1360, http://dx.doi.org/10.1126/science.1113193.

Figure captions

Figure 1. (a) Paths of PKiKP (gray) and PKPdf (black) at 135°, and PKPbc (gray) and PKPdf at 151°. (b) Map view of differential time residuals of PKiKP–PKPdf. PKPdf rays in the inner core (IC) along equatorial ($\xi \geq 40°$) and polar ($\xi < 40°$) paths are indicated by gray dotted and black solid lines, respectively. Locations of df turning points in the IC for equatorial and polar paths are indicated by small circles and large triangles, respectively. *dt*(*PKiKP–PKPdf*) values are plotted at df turning locations, with magnitudes indicated by color bars. The western hemispheric boundary (WHB) is indicated by a yellow solid and black dotted line. Derivations of the WHB's position are discussed in the text. (c) Map view of PKP(bc–df) for df sampling the deeper part of the IC, shown on a Lambert azimuthal equal-area projection centered at 50°N, 170°W.

Figure 2. (a) Differential time residuals of PKiKP–PKPdf relative to AK135, denoted *dt*(*PKiKP–PKPdf*), as a function of PKPdf turning longitude (φ). (b) Differential time residuals of PKP(bc–df) relative to AK135, denoted *dt*(*bc–df*), as a function of φ. The eastern hemisphere (EH) and western hemisphere (WH) of the IC sampled by df are defined by the WHB. Means of *dt* in 5° longitudinal bins are indicated by diamonds. Symbols of *dt* for the EH and WH along equatorial (equ) and polar (pol) raypaths are displayed in the legend. In (b), *dt*(*bc–df*) are further corrected for the time shift due to heterogeneous mantle structures predicted by the GyPSuM P-wave tomographic model. The green dotted line indicates the derived lateral gradients of 0.002 s/° decreasing westward from 155°E to 160°W in the EH and of 0.012 s/° decreasing westward from 160°W to 130°W in the WH.

Figure 3. PKiKP–PKPdf waveforms selected at similar distances to display longitudinally dependent anisotropy in the region 180–155°W. Waveforms are band-pass filtered from 0.5 to 2.0 Hz, and aligned with the maximum amplitude of the PKiKP phase ($t = 0$). The maximum amplitude of the picked df and the AK135 model's predicted df arrival are indicated by black and gray vertical lines, respectively. The text identifier below and to the left of each waveform follows the format trace number, event date–station code, epicentral distance (Δ), source depth (km), df turning longitude (φ), df angle relative to the Earth's rotation axis (ξ), and traveltime residual (*dt*, s). Traces 1–3 refer to φ near 180°W, traces 4–7 to φ in the range 175–170°W, and traces 8–10 to φ of 168–144°W.

Figure 4. Differential time residuals *dt*(*PKiKP–PKPdf*), computed relative to AK135, as a function of ξ (PKPdf angle relative to the Earth's rotation axis, ERA) for df sampling of the (a) western and (b) eastern hemispheres of the uppermost 80 km of the IC. Polar and equatorial paths are defined by $\xi < 40°$ and $\xi \geq 40°$, respectively. Symbols of *dt* are identical to those displayed in Fig. 2. Anisotropy is fitted using Equation (1). (a) Beneath the WH, in the longitude range spanning 180–155°W, a moderate anisotropy of 1.75% is determined by α, ε, and γ with best-fit values of −0.13, 1.75, and −0.95, respectively (black line). (b) Beneath the EH, in the range spanning 160°E–180°W, a nearly isotropic velocity (anisotropy of 0.25%) is determined by α, ε, and γ with best-fit values of −0.04, 0.25, and −0.08, respectively (gray line).

Figure 5. Differential time residuals *dt*(*PKiKP–PKPdf*) computed relative to the mE2 and mW2 composite models of the IC, plotted as a function of φ, for PKPdf sampling along equatorial paths, to assess the uncertainties in *dt*(*PKiKP–PKPdf*) due to laterally shifting the position of the WHB. For a fixed WHB, the length and time of the df ray confined in the EH and WH of the IC can be estimated. The entire df time in the IC consists of the portion confined in the EH (predicted by the mE2 model, Fig. S2) and WH (predicted by mW2). This allows us to consider the effect of df time traversing the east–west (EW) inter-hemispheres of the IC, and thus estimate quantitative uncertainties in *dt* due to a lateral shift in the position of the WHB, which yields a more reliable estimate of the true position of the WHB. The laterally shifted positions of the WHB are tested at (a) 170°E, (b) 180°W, (c) 170°W, (d) 160°W, (e) 150°W, and (f) 140°W. Means of *dt* in 5° longitudinal bins are indicated by diamonds. The symbols for *dt* are identical to those displayed in Fig. 2. (g) Means and (h) root-mean-square (RMS) residuals of *dt* as a result of the WHB shifting from 170°E–140°W, computed in 10° longitudinal bins. The values of the means (g) and RMS residuals (h) are displayed side-by-side and distinguished by color (color legend in (h)) for comparison. The optimal position of the WHB is at 170–160°W (light blue and red bars), providing minimum values across longitudinal bins 170°E–160°W (highlighted by the arrows in (g) and (h)).

Figure 6. Differential time residuals *dt*(*PKiKP–PKPdf*) plotted as a function of φ, for PKPdf phases sampling along polar paths, similar to Fig. 5 for equatorial paths. The laterally shifted positions of the WHB are tested at (a) 170°E, (b) 180°W, (c) 170°W, (d) 160°W, (e) 150°W, and (f) 140°W. Means of *dt* in 5° longitudinal bins are indicated by diamonds. The symbols for *dt* are identical to those displayed in Fig. 2. (g) Means and (h) RMS residuals of *dt* as a result of the WHB shifting from 170°E–140°W, computed in 10° longitudinal bins. The values of the means (g) and RMS residuals (h) are displayed side-by-side and distinguished by color (color legend in (h)) for comparison. An increase in means (g) and RMS residuals (h) of *dt*(*PKiKP–PKPdf*) occurred across 180°W, placing the WHB at 180°W.

Figure 7. Analysis of the latitude dependence on the WHB, derived from *dt*(*PKiKP–PKPdf*) for PKPdf phases sampling along equatorial paths. The df ray turning latitudes for the northern (a, b) and southern (c, d) hemispheres of the IC are analyzed separately, with a north–south division placed at 8°N. In the northern hemisphere (8–90°N), the placement of the WHB at 170–160°W (light blue and red bars in (a) and (b)) often yielded minimal means and RMS residuals of *dt* over longitudinal bins 180–160°W (highlighted by the arrows in (a) and (b)). In the southern hemisphere (90°S–8°N), the placement of the WHB at 180–170°W (gray and light blue bars in (c) and (d)) often yielded minimal means but similar RMS residuals over longitudinal bins 180–160°W (highlighted by the arrows in (c) and (d)).

Figure 8. Analysis of the latitude dependence on the WHB, derived from *dt*(*PKiKP–PKPdf*) for PKPdf phases sampling along polar paths, similar to Fig. 7 for equatorial paths. In the northern hemisphere (8–90°N), the placement of the WHB at 170°W yielded comparable minima in the means and RMS residuals of *dt* over longitudinal bins 160°E–180°W of the EH and over longitudinal bins 170–160°W of the WH (arrows in (a) and (b)). In the southern hemisphere (90°S–8°N), the placement of the WHB at 180°W can optimally distinguish the means and RMS residuals of *dt* over 160°E–180°W of the EH and 180–160°W of the WH (arrows in (c) and (d)).

Figure 9. Inferred latitudinal dependence of the WHB and isotropic velocity/anisotropy contrast across the WHB. Each image is shown on a Lambert azimuthal equal-area projection centered at 50°N, 170°W. The yellow solid line with black dots indicates the inferred position of the WHB. The percentages refer to the difference between our modeled velocity structure and that of the AK135 model, with blue and red values indicating higher and lower modeled velocities, respectively. (a) Isotropic structures in the uppermost 80 km of the IC. The estimated isotropic velocity contrast near the WHB is lower than previous estimates for the bulk part of the EH and WH. (b) Anisotropic structures in the uppermost 80 km of the IC. In the northern hemisphere, the WHB is placed at 170°W, compared with 160°W in (a). (c) Isotropic structures in the upper 300 km of the IC. The isotropic velocity contrast estimated near the WHB is lower than previous estimates for the bulk part of the EH and WH at depth.

Table 1. Summary of the means and 1σ uncertainties of *dt*(*PKiKP–PKPdf*) for PKPdf sampling the eastern and western hemispheres and along equatorial and polar raypaths of the IC

Region (PKPdf ray direction)	Means ± 1 σ uncertainties
160°E–170°W, eastern hemisphere (equatorial)	+0.05 s ± 0.05 s
160°E–175°E, eastern hemisphere (polar)	+0.2 s ± 0.08 s
170–130°W, western hemisphere (equatorial)	−0.2 s ± 0.12 s
175°E–155°W, western hemisphere (polar)	+0.89 s ± 0.21 s

Table 2. Summary of the inferred WHB position, using different PKP differential time data (bold cases indicate the WHB position determined by the primary dataset).

Region	WHB position determined from equatorial data	WHB position determined from polar data
Northern hemisphere (8–90°N)	**170–160°W (using PKiKP–PKPdf)**	170°W (using PKiKP–PKPdf)
Southern hemisphere (90°S–8°N)	180–170°W (using PKiKP–PKPdf)	**180°W (using PKiKP–PKPdf)**
Northern hemisphere (8–90°N)	**170–160°W (using PKP(bc–df))**	

Highlights

- PKiKP–PKPdf and PKP(bc–df) are used to probe the Inner Core (IC) EW transition
- The western hemispheric boundary (WHB) of the IC is latitudinally dependent
- The uppermost IC beneath the Pacific Ocean of the WH exhibits 1.75% anisotropy
- The lower isotropic velocity contrast is observed near the WHB of the IC

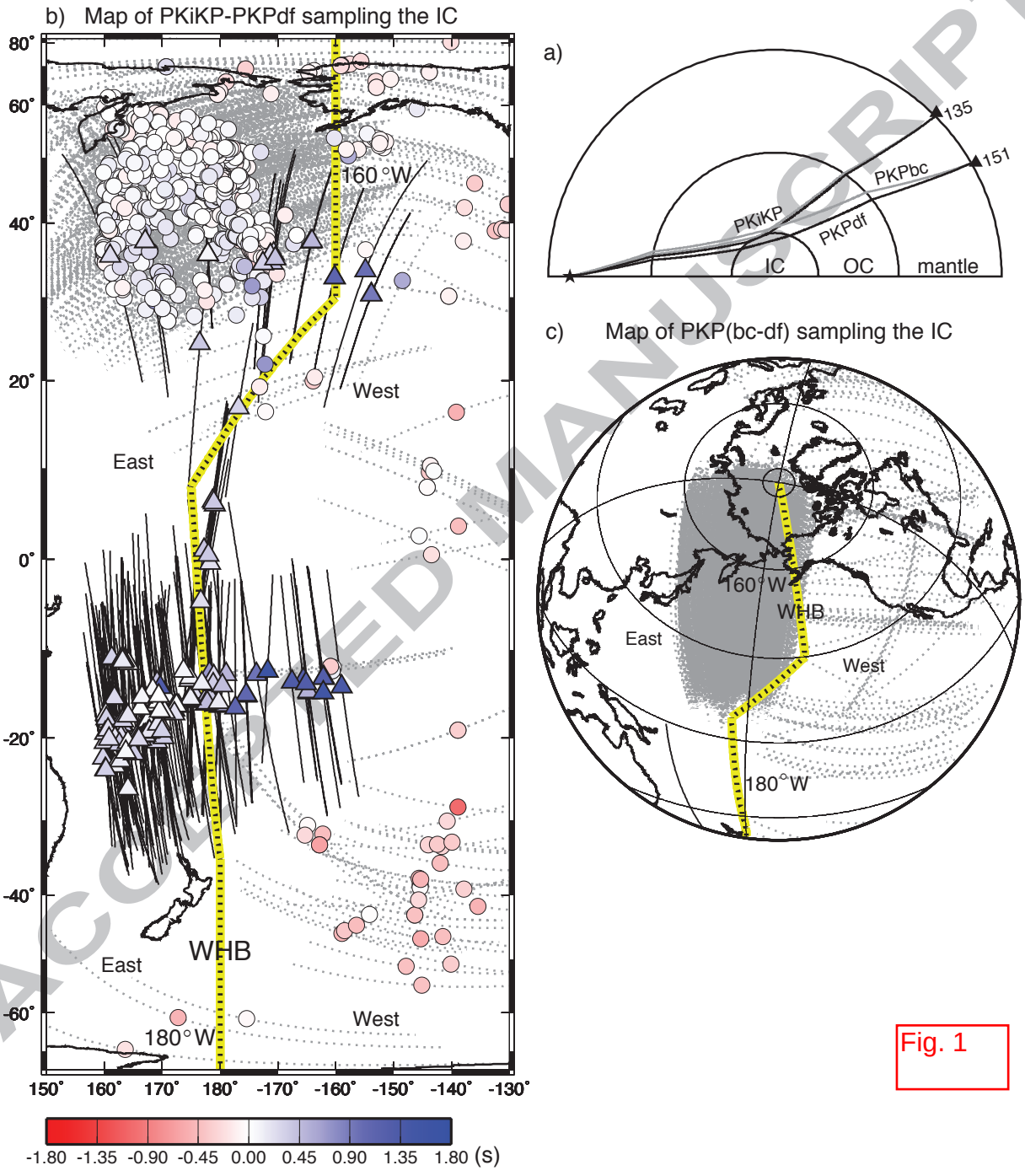

Fig. 1

Fig. 2

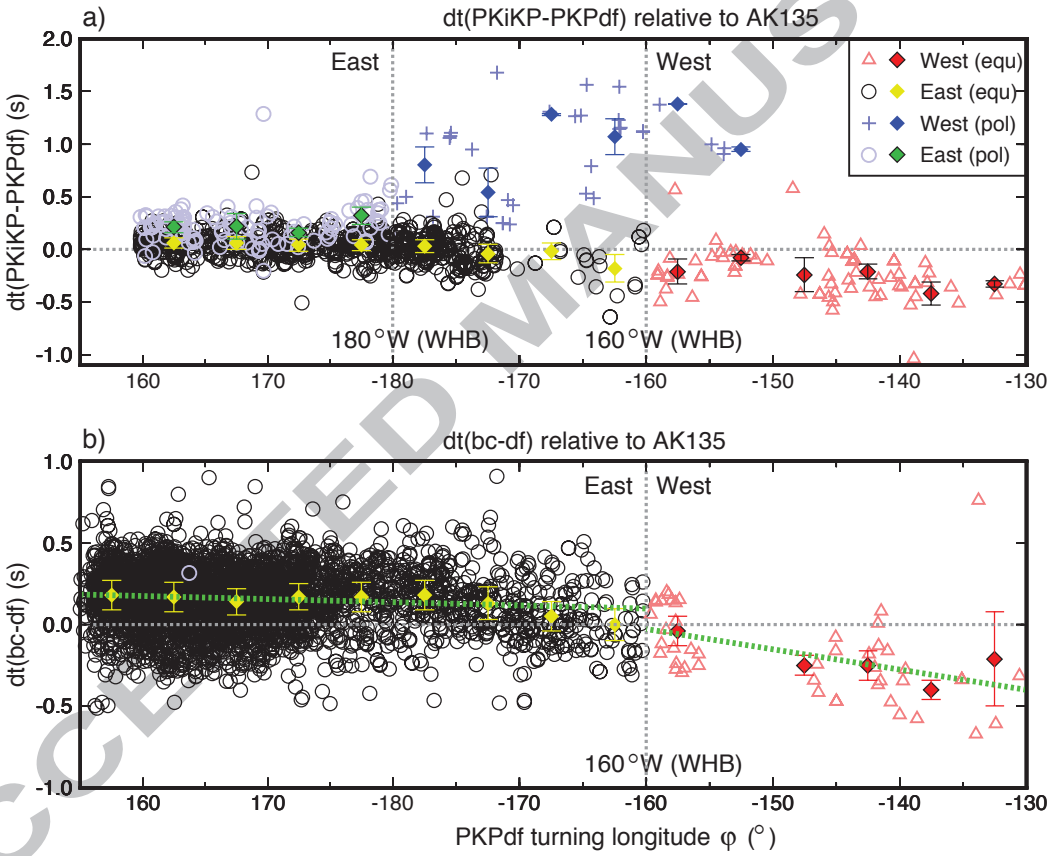

Fig. 3

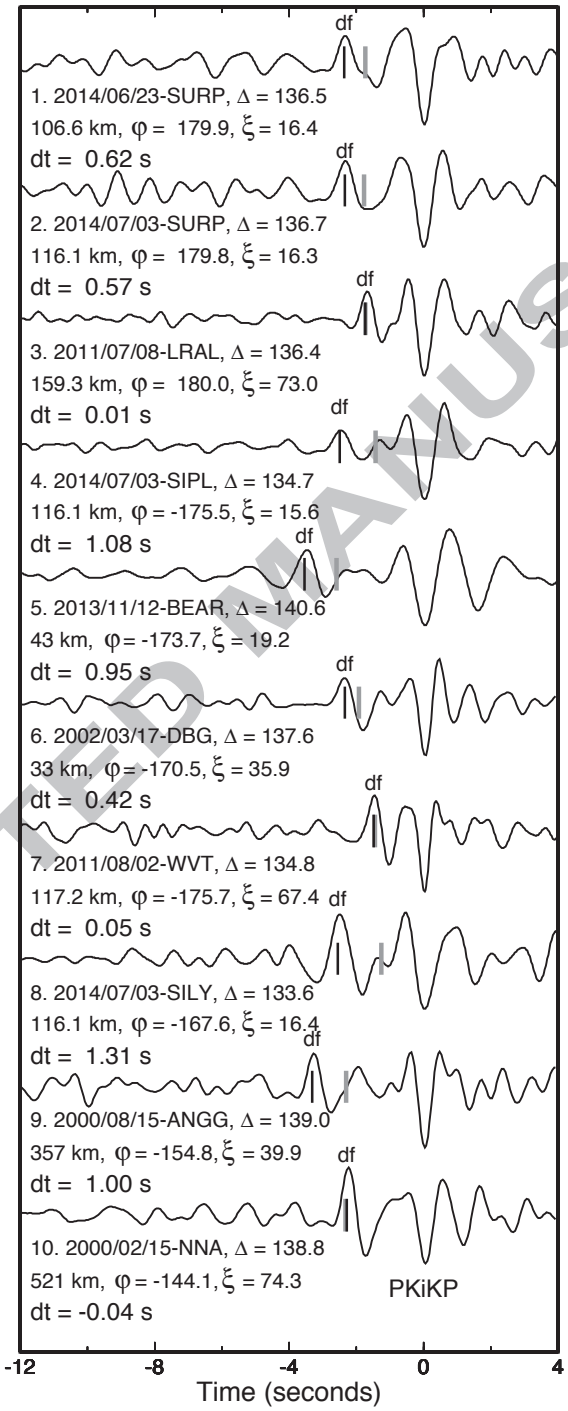

Fig. 4

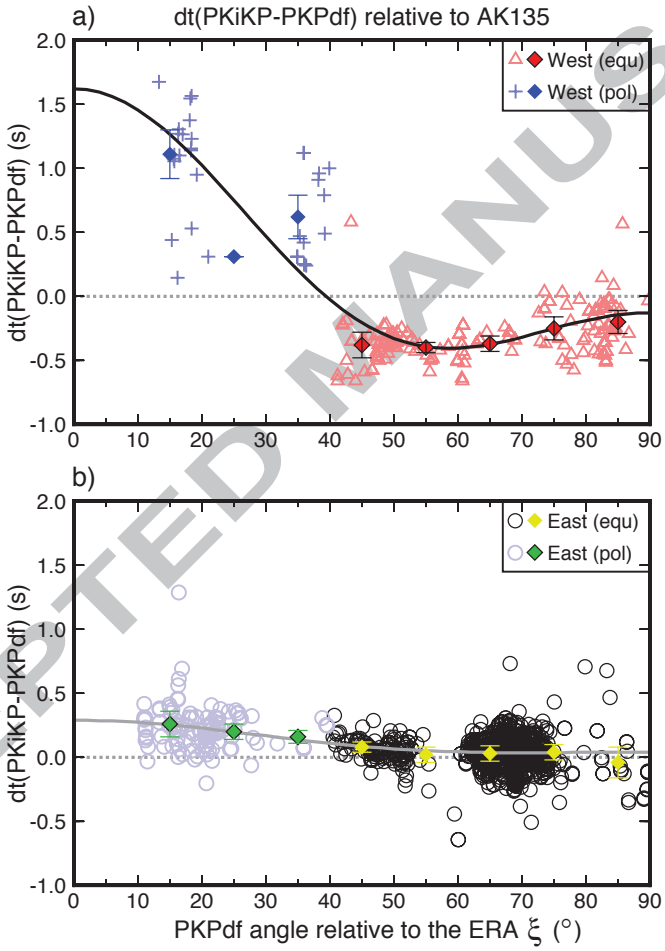

Fig. 5

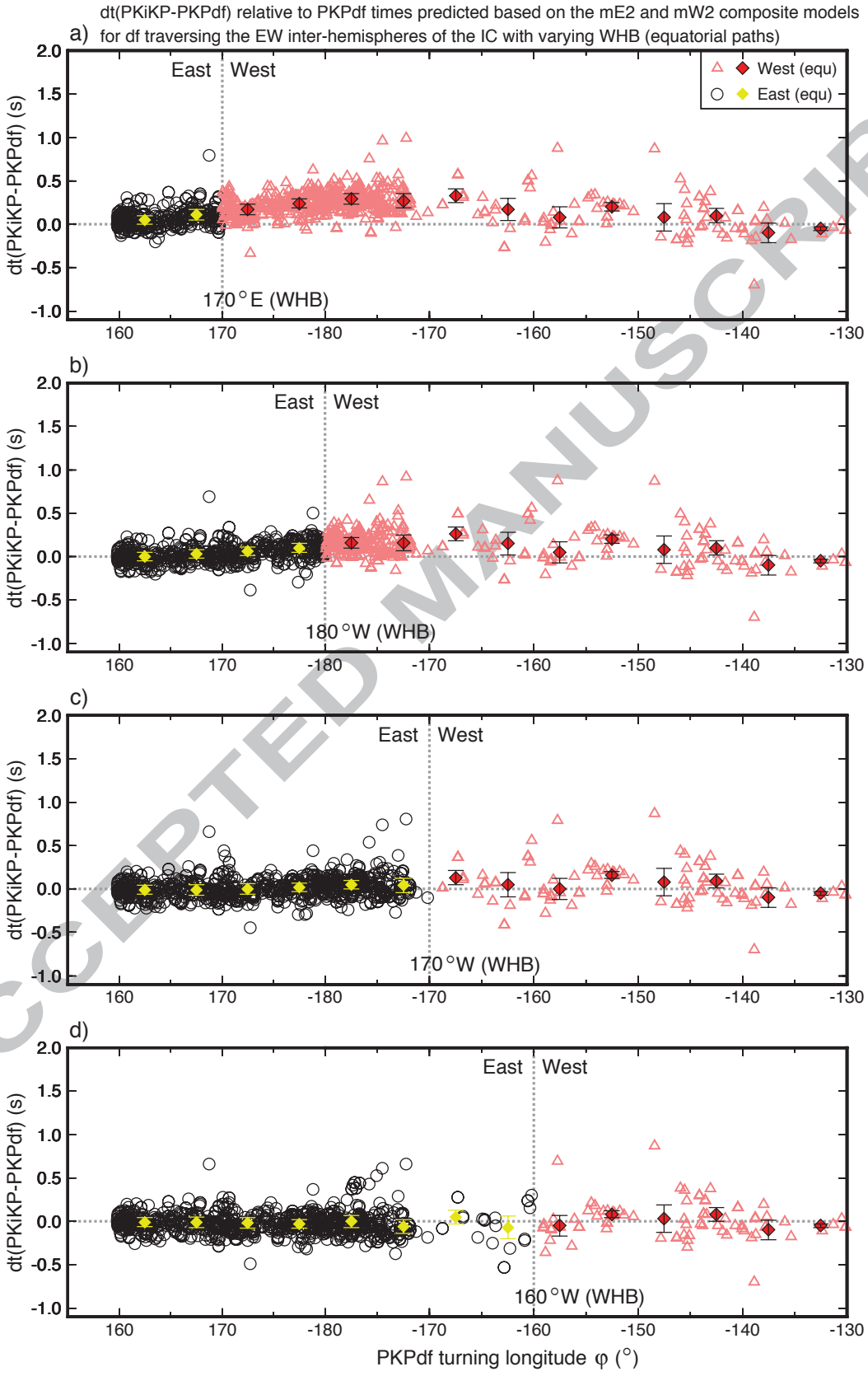

Fig. 5

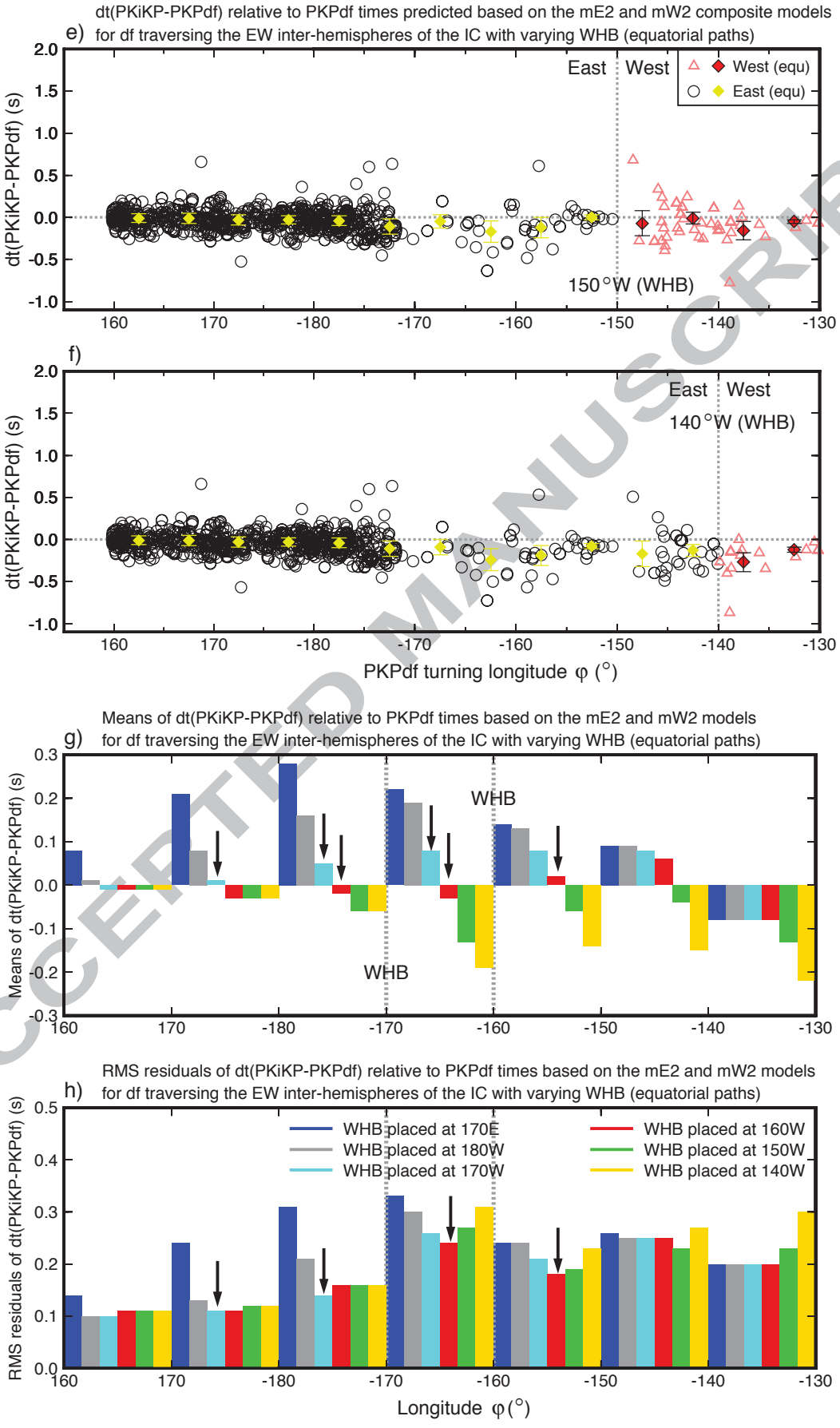

Fig. 6

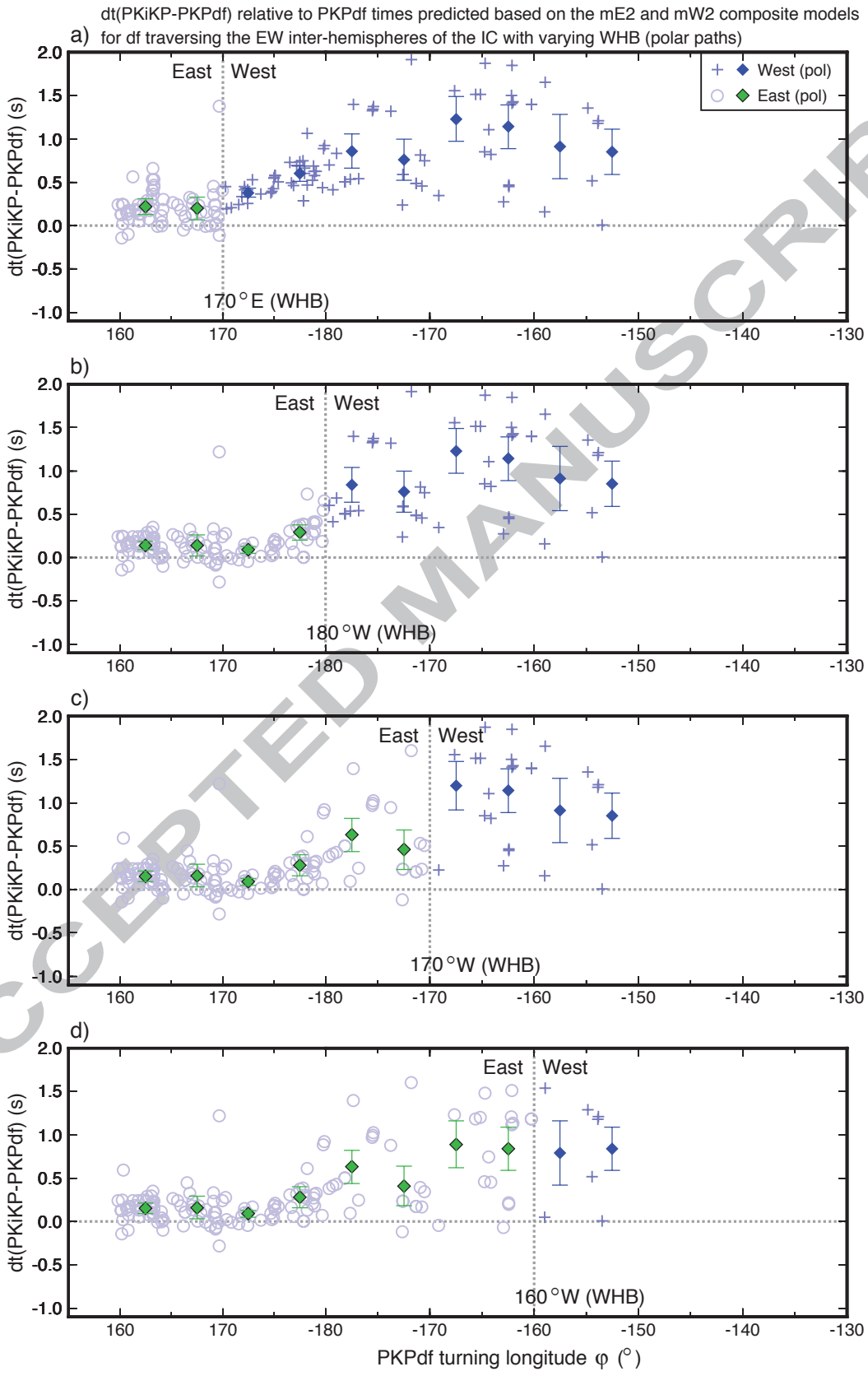

Fig. 6

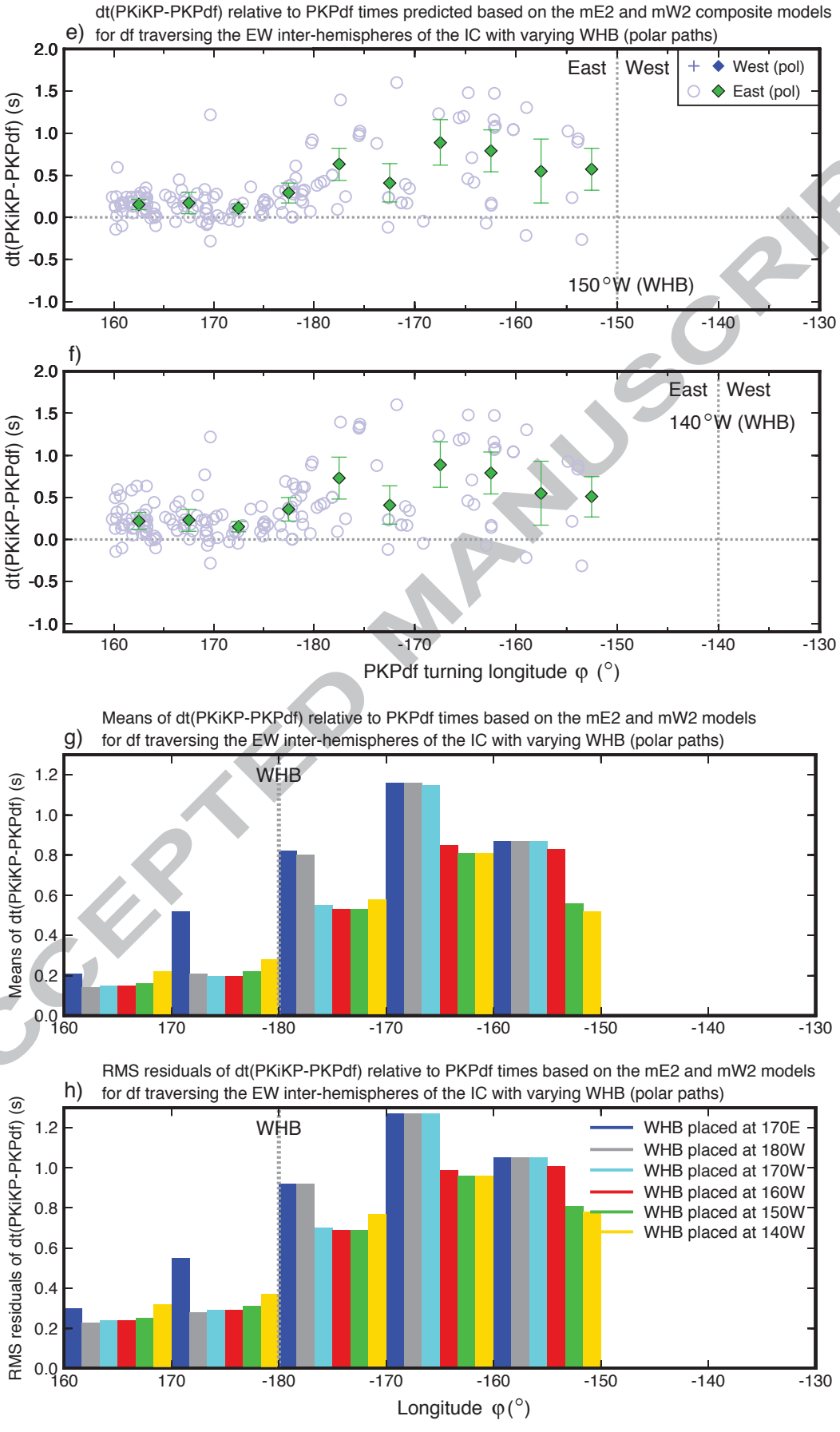

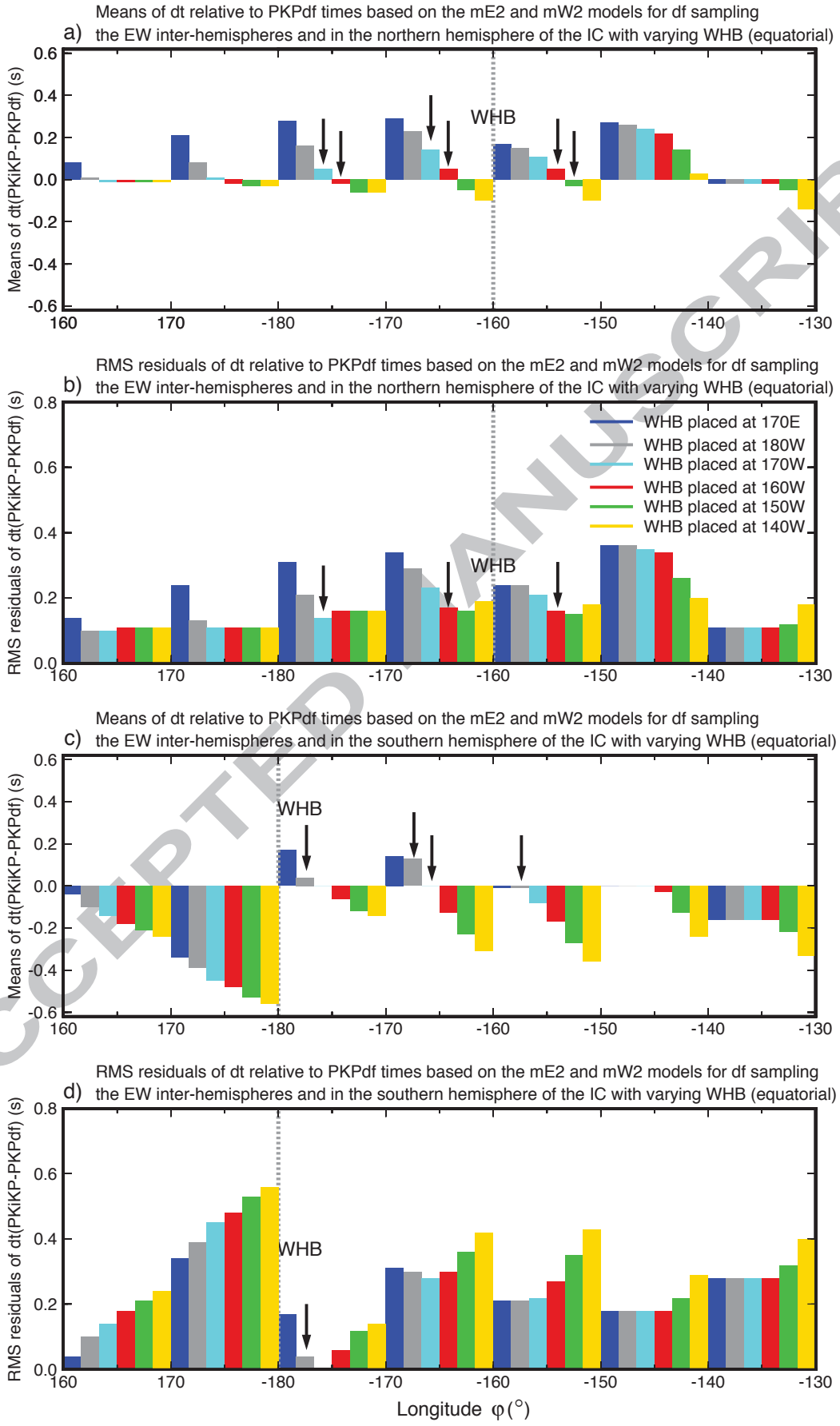

Fig. 7

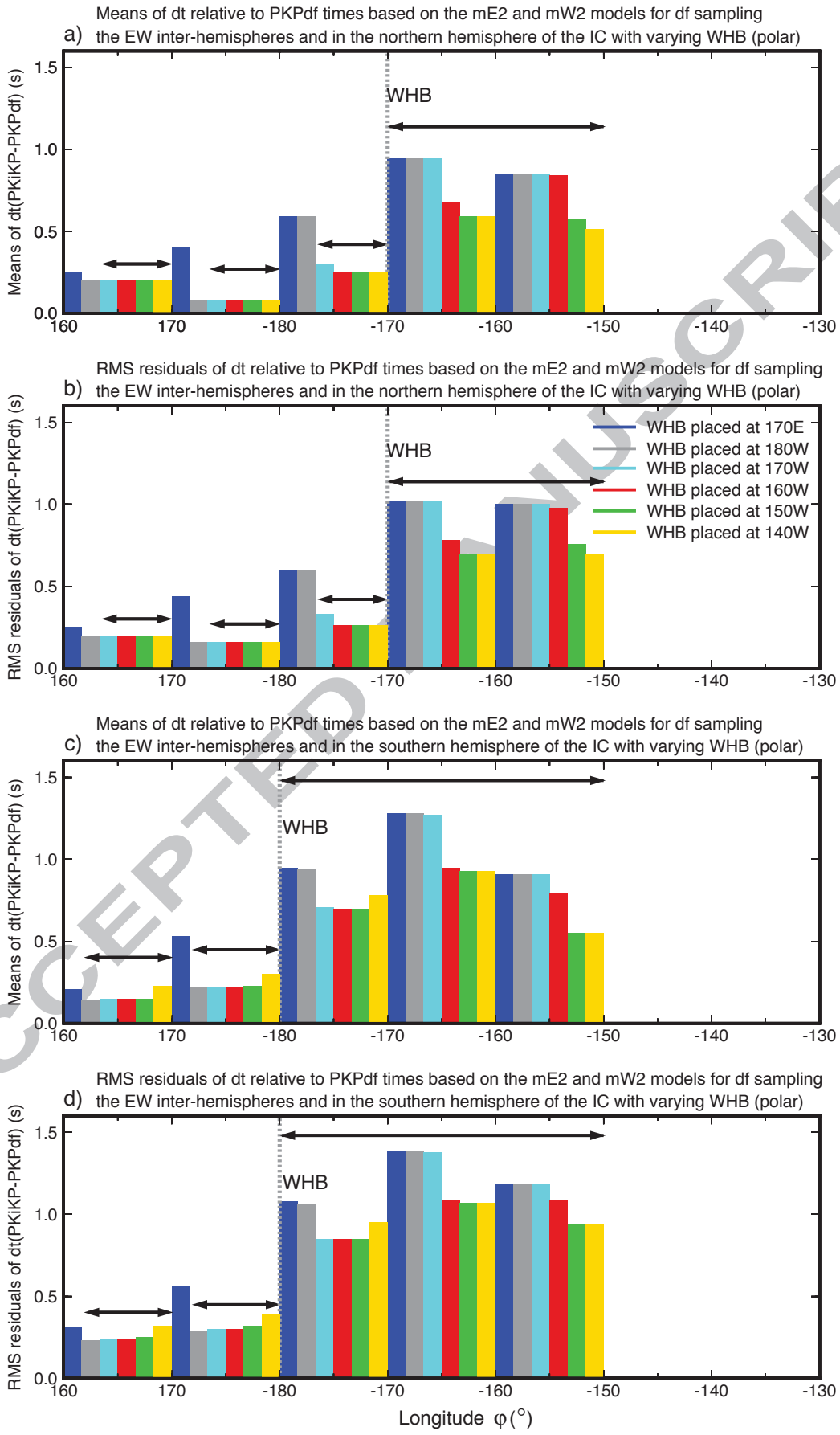

Fig. 8

Fig. 9

a) Isotropy in the uppermost 80 km of the IC

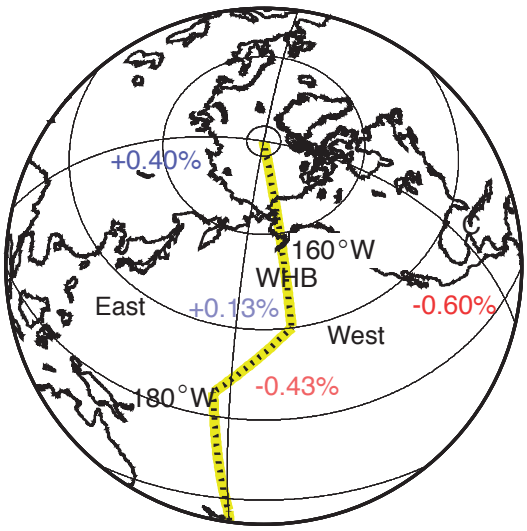

b) Anisotropy in the uppermost 80 km of the IC

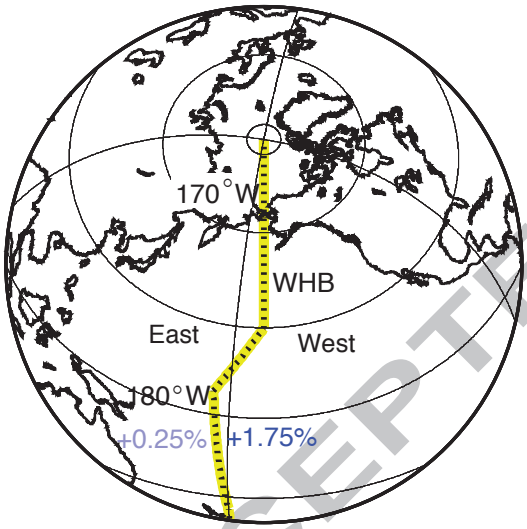

c) Isotropy in the upper 300 km of the IC